

Article

# A Visual Investigation of CO<sub>2</sub> Convective Mixing in Water and Oil at the Pore Scale Using a Micromodel Apparatus at Reservoir Conditions

Widuramina Amarasinghe <sup>1,2,\*</sup>, Seyed Farzaneh <sup>3</sup>, Ingebret Fjelde <sup>1</sup> , Mehran Sohrabi <sup>3</sup> and Ying Guo <sup>1,2</sup>

<sup>1</sup> NORCE Norwegian Research Center AS, P.O. Box 8046, 4068 Stavanger, Norway; infj@norceresearch.no (I.F.); yigu@norceresearch.no (Y.G.)

<sup>2</sup> Department of Energy Resources, University of Stavanger, P.O. Box 8600, 4036 Stavanger, Norway

<sup>3</sup> Centre for Enhanced Oil Recovery and CO<sub>2</sub> Solutions, Heriot-Watt University, Edinburgh EH14 4AS, UK; Amir.Farzaneh@hw.ac.uk (S.F.); M.Sohrabi@hw.ac.uk (M.S.)

\* Correspondence: widuramina@norceresearch.no

Received: 9 December 2020; Accepted: 26 January 2021; Published: 28 January 2021



**Abstract:** CO<sub>2</sub> convective mixing in water has been visualized in Hele-Shaw and PVT cell experiments but not at the pore scale. Furthermore, CO<sub>2</sub> convective mixing in a three-phase system (i.e., CO<sub>2</sub> in the presence of both water and oil) has not been visually investigated. A vertically placed micromodel setup was used to visualize CO<sub>2</sub> convective mixing at 100 bar and 50 °C, representative of reservoir conditions. To the best of our knowledge, for the first time, we have visually investigated CO<sub>2</sub> convective mixing in water at the pore scale and also CO<sub>2</sub> convective mixing in a multiphase system (water and oil). CO<sub>2</sub> mixing in water governed by both diffusion and convection mechanisms was observed. The vertical CO<sub>2</sub> transport velocity was calculated to be 0.3 mm/min in both a 100% water saturation system and a residual oil-saturated system. First, CO<sub>2</sub> always found the easiest path through the connected pores, and then CO<sub>2</sub> was transported into less connected pores and dead-end pores. CO<sub>2</sub> transport into dead-end pores was slower than through the preferential path. CO<sub>2</sub> transport into water-filled ganglia with trapped oil was observed and was slower than in water.

**Keywords:** CO<sub>2</sub> storage; CO<sub>2</sub> convective mixing; water and oil; micromodel; reservoir conditions

## 1. Introduction

Underground CO<sub>2</sub> storage in aquifers, oil, and gas reservoirs has huge potential to mitigate climate change [1–4]. Many challenges such as storage location identification, CO<sub>2</sub> injection, CO<sub>2</sub> monitoring, financial viability, and public awareness need to be overcome to make CO<sub>2</sub> geological storage viable [5,6]. The introduction of enhanced oil recovery (EOR) processes has made CO<sub>2</sub> storage in oil reservoirs more financially viable with more demanding technical details [7,8].

When CO<sub>2</sub> is injected into an aquifer or oil and gas reservoirs, the gas creates a plume under the caprock or gas cap. The CO<sub>2</sub> from this plume mixes with the fluids (water and oil) present in the reservoir, initially through diffusion. This increases the density of the fluid mixture, which leads to gravity-driven convective mixing [9–11] (see Figure 1). An understanding of the convective mixing process at the laboratory scale is essential to develop, validate, and scale up computational models for CO<sub>2</sub> storage [12–15].

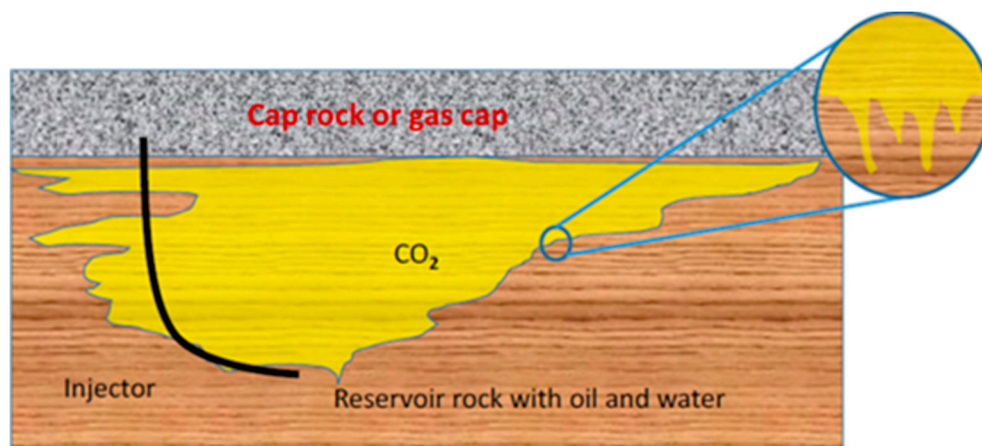


**Figure 1.** Simplified sketch of convection-driving dissolution of CO<sub>2</sub> with oil inside the reservoir.

In the literature, several CO<sub>2</sub> convective mixing experiments have been reported with water or brine. Two-dimensional (2D) Hele-Shaw visualization experiments have been conducted without the presence of porous media [16–21] and also with the presence of porous media [22–24]. In these studies, pH dye indicators were used to visualize the spatial distribution of different concentrations of CO<sub>2</sub> in the aqueous solution. Among the studies, only Amarasinghe, et al. [22] conducted experiments under reservoir conditions with porous media. Furthermore, Khosrokhavar, et al. [18] and Amarasinghe, et al. [25] studied CO<sub>2</sub> convective mixing in oleic phases. A detailed review of CO<sub>2</sub> convective mixing experiments was conducted by Amarasinghe, et al. [22]. Moreover, in the literature, CO<sub>2</sub> convective visualization experiments have not been carried out in a three-phase system (i.e., with CO<sub>2</sub>, water, and oil) at any scale.

It is important to understand how CO<sub>2</sub> convective mixing occurs at the pore scale. In the literature, there is a lack of experimental results with visualizations of CO<sub>2</sub> convective mixing; therefore, micromodel visualization experiments are needed. Micromodel experiments are essential for direct visualization of fluid flow and mixing at the pore scale [26–39]. With the help of micromodel experiments, CO<sub>2</sub> diffusion and convective mixing into different pore arrangements can be investigated. Morais, et al. [40] conducted an extensive review of key processes related to CO<sub>2</sub> underground storage at the pore scale using high-pressure micromodels. In this experimental study, we observed CO<sub>2</sub> convective mixing, using a micromodel apparatus at reservoir representative pressure and temperature conditions (i.e., at 100 bar and 50 °C, respectively), in both a 100% water saturation system and a residual oil-saturated system.

## 2. Experimental Method

### 2.1. Experimental Setup

Experiments were carried out in a high-pressure/temperature micromodel setup. The test pressure and temperature were 100 bar and 50 °C, respectively; hence, CO<sub>2</sub> was in the supercritical phase. A schematic diagram of the experimental setup is shown in Figure 2. Distilled water with 4 wt% bromothymol blue pH indicator was used as the water solution. n-Decane was used as the oil and Sudan Red B was used as an oil-soluble dye in the n-decane phase. The experimental setup consisted of three piston cells for water, CO<sub>2</sub>, and n-decane. Another piston cell was used as a retraction cell. All piston cells were placed inside an oven. The micromodel setup was vertically oriented inside a housing chamber with a constant temperature, where the micromodel was submerged in a confining fluid (water) at a pressure of 170 bar, creating an overburden pressure of 70 bar.

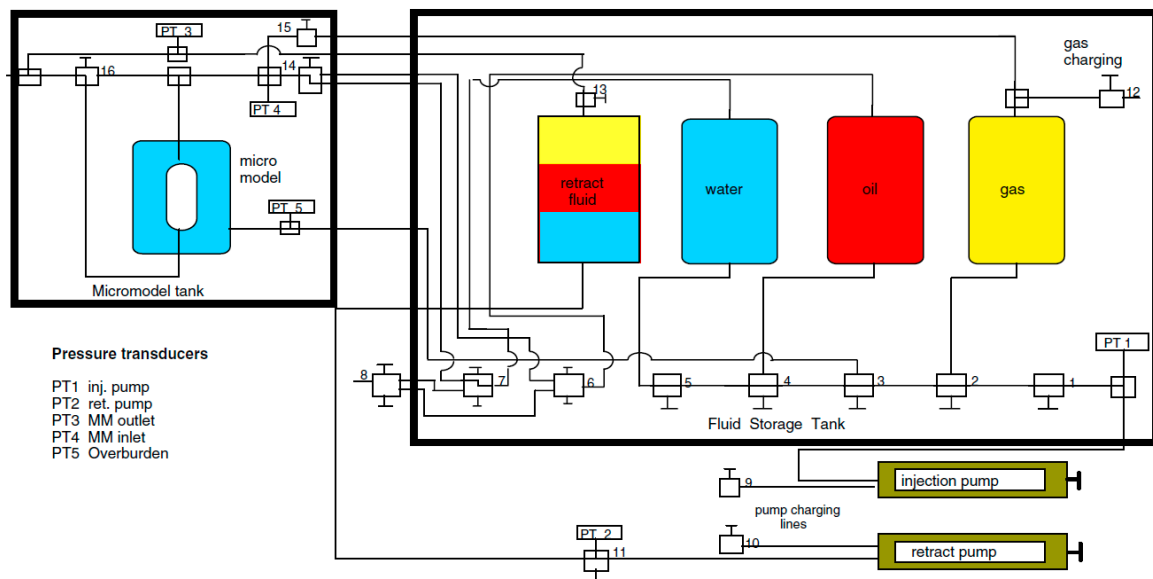


**Figure 2.** Schematic piping and instrumentation (P&ID) diagram of the experimental setup [31].

The micromodel was prepared by placing a flat glass plate over a second glass plate that had a 2D etched pore structure (see Figure 3). Chemical treatment was used to etch the 2D pore structure on the second glass plate. The pore structure used is a prearranged pore structure, inspired by a cross-section of a North Sea reservoir rock, which is only one pore deep, making it possible to observe fluids as they flow through the pores in a 2D environment. The final micromodel pore structure consisted of two triangles at the top and bottom, as shown in Figure 4, to facilitate a free space for the fluid that was introduced into the pores. A hole was drilled at the top and the bottom of each micromodel glass plate, for the inlet and outlet of fluids (see Figure 3). The dimensions and important properties of the micromodel are given in Table 1. More details of the experimental setup are presented by Sohrabi, et al. [31,41], and Mahzari, et al. [28]. The design of the micromodel setup allowed us to visualize CO<sub>2</sub>–fluid interactions at the pore scale while investigating the effects of pore structure and boundary conditions during CO<sub>2</sub> mixing.

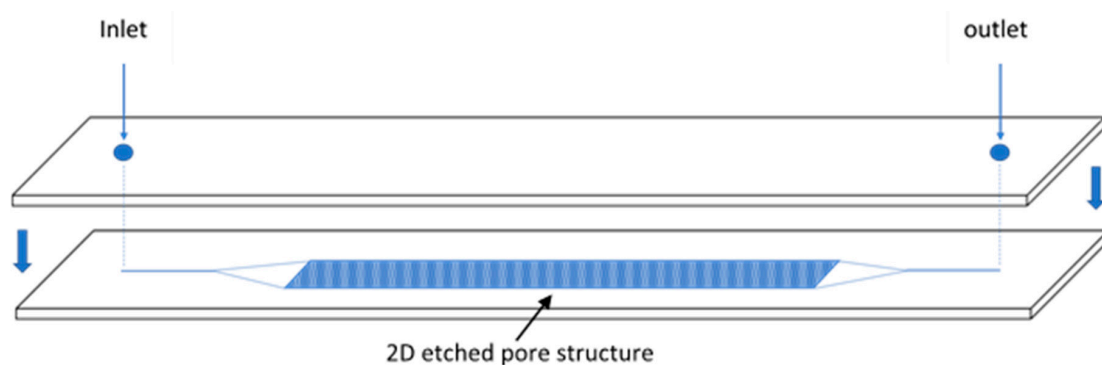


**Figure 3.** Sketch of the two-dimensional (2D) etched pore structure glass plate and flat glass plate design.

Table 1. Properties of the micromodel.

Total Height	Height from Top Pore to Bottom Pore ( $H$ )	Width	The Average Depth of Pores	Pore Volume	Porosity ( $\Phi$ )	Permeability( $k$ )	Wettability
70 mm	51.2 mm	7 mm	40 $\mu\text{m}$	0.01 $\text{cm}^3$	0.61	10 D	Water-wet

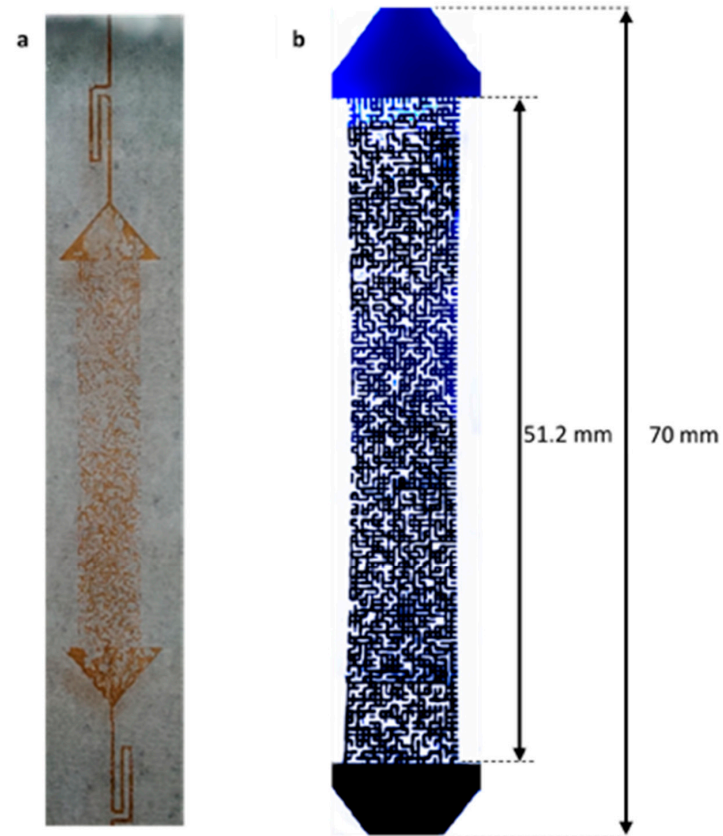


**Figure 4.** (a) Front view image (real view) of the etched pore structure on the glass; (b) a detailed digital image of the pore structure of the complete micromodel, when it is 100% saturated with water solution.

Quizix Q5000 precision pumps were used to control the injection, retraction, and the pressure of the fluids during the experiments. An adjustable magnifying camera system, with a 400× zoom lens, was used for the acquisition of the images/videos of the entire micromodel during the experiments. A schematic sketch of the camera system is shown in Figure 5. ImageJ open-source image analysis software [42] was used to analyze the local velocities of CO<sub>2</sub> transport inside the pores.

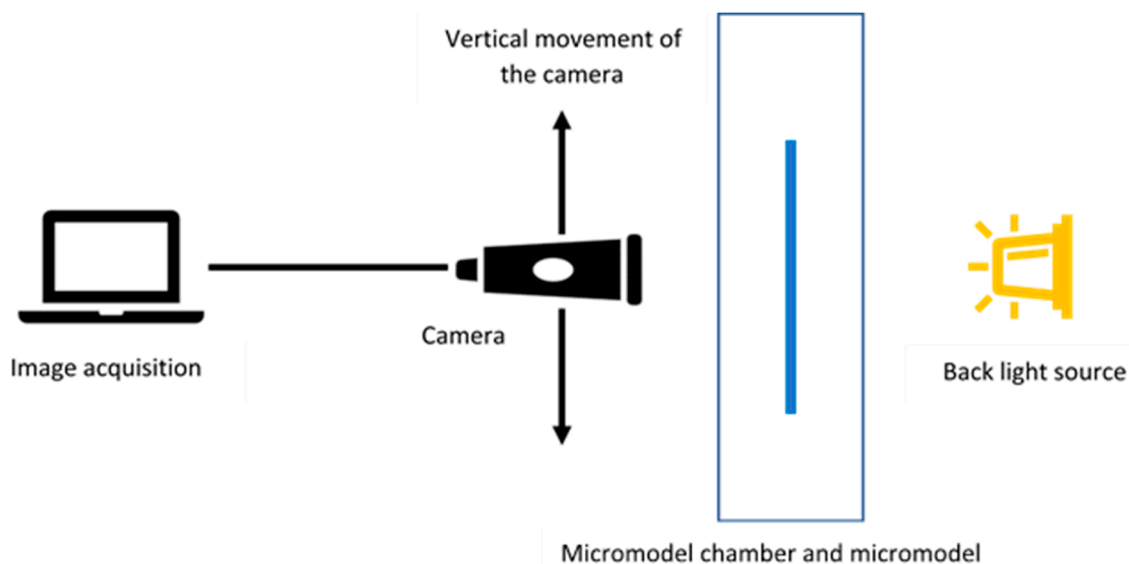


Figure 5. Schematic sketch of the image acquisition system.

## 2.2. Experimental Cases

Two different sets of experiments were carried out to investigate CO<sub>2</sub> mixing in water and oil inside the micromodel (see Table 2).

Table 2. Set of experimental cases.

Case #	The Initial Condition of the Micromodel
1	100% water saturation
2	Residual oil saturation ( $S_{or}$ )

## 2.3. Experimental Procedure

The valve system connected to the micromodel is described in the following experimental procedure (Figure 6). For all the experiments, first, the micromodel was 100% saturated with the water solution. A slow injection rate of 0.01 cm<sup>3</sup>/h was used to obtain the correct saturation.

In Case 1, CO<sub>2</sub> was injected from the top through the bypass (V1 open) at a rate of 0.01 cm<sup>3</sup>/h for a few hours, while the bottom valve was kept open (V2 open). The retraction of the fluids was carried out using the same rate of 0.01 cm<sup>3</sup>/h. Then, the bypass was closed (V1 close), and CO<sub>2</sub> was injected into the micromodel at a rate of 0.01 cm<sup>3</sup>/h (with the retraction from bottom) until CO<sub>2</sub> mixing in water was initiated in the triangular area (see Figure 7). Then, the injection of CO<sub>2</sub> into the micromodel was stopped and the bypass was opened (V1 open) and CO<sub>2</sub> continued to be injected through the bypass at a retraction rate of 0.01 cm<sup>3</sup>/h. The mixing of CO<sub>2</sub> inside the micromodel was captured using the camera system.

In Case 2, after 100% saturation of water was established, n-decane was injected at a rate of 0.01 cm<sup>3</sup>/h from the bottom of the micromodel to establish initial water saturation ( $S_{wi}$ ). Then, water was injected from the top of the micromodel at a rate of 0.01 cm<sup>3</sup>/h to establish residual oil saturation ( $S_{or}$ ). After ensuring that  $S_{or}$  was established through observation, the micromodel was scanned again.

Then, the same procedure was followed as in Case 1. CO<sub>2</sub> did not invade the pores with the by-pass open (V1 open), because oil ganglia were blocking the pores. Hence, to investigate CO<sub>2</sub> mixing in the pore spaces, CO<sub>2</sub> was injected into the micromodel at a rate of 0.005 cm<sup>3</sup>/h with the bypass closed and the retraction of fluid from the bottom. When CO<sub>2</sub> had invaded the micromodel halfway, the pump was stopped and CO<sub>2</sub> mixing in water was observed.

It should be noted that the actual color of the pH indicator was blue at a higher pH (pH > 7.6) and yellow at a lower pH (pH < 6). The real n-decane phase color was dark red. Due to the camera system and the presence of backlight, a dark black color represented the water phase at a higher pH and a light blue color represented the water phase after pH reduction by CO<sub>2</sub> (see Figure 7), while a dark blue color represented the oil phase (see Figures 13 and 14).

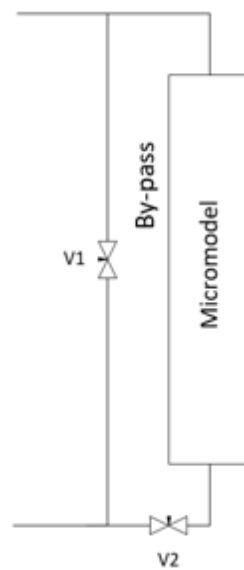


Figure 6. Valve system connected to the micromodel.

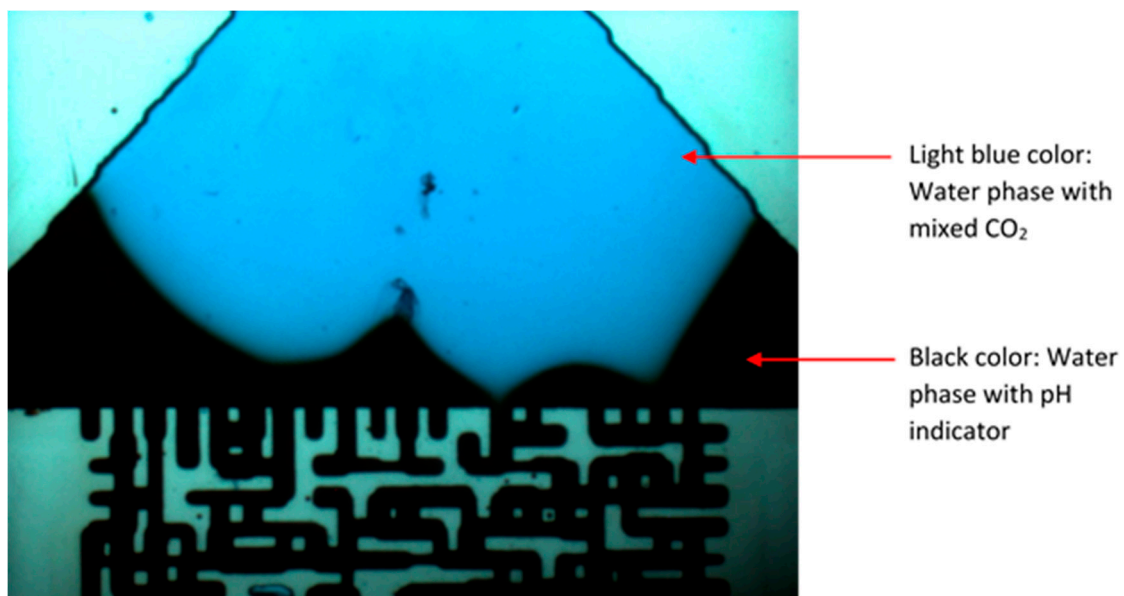


Figure 7. CO<sub>2</sub> in the triangle area when CO<sub>2</sub> injection into the micromodel was stopped.

#### 2.4. Rayleigh ( $Ra$ ) Number Calculation

In theory, the Rayleigh ( $Ra$ ) number, which is a dimensionless number that represents the ratio between free convection and diffusion, should be equal to or greater than  $Ra_{critical}$ ,  $4\pi^2$  (39.47) for the natural convection to become substantial [10,43].

The  $Ra$  number was calculated using the equation  $Ra = (\Delta\rho gkH)/(\mu D\Phi)$ , where  $\Delta\rho$  is the density increase in fluid (water or oil) due to  $CO_2$  dissolution,  $g$  is the acceleration of gravity,  $k$  is the permeability of the porous media,  $H$  is the height of porous media,  $\mu$  is the dynamic viscosity of the fluid,  $D$  is the molecular diffusion coefficient of  $CO_2$  in fluid, and " $\Phi$ " is the porosity of the porous media. The parameter values used to calculate the  $Ra$  number are given in Tables 1 and 3. The  $Ra$  number was calculated considering 100% water saturation ( $Ra_{100\% \text{ water saturation}}$ ) and 100% oil saturation ( $Ra_{100\% \text{ oil saturation}}$ ).

**Table 3.** Parameters for the Rayleigh ( $Ra$ ) number calculation.

Parameter	Value *		Units
$\rho_{CO_2}$	384.67		kg/m <sup>3</sup>
	<b>Water</b>	<b><i>n</i>-decane</b>	
$\rho_{fluid}$	988.05	730	kg/m <sup>3</sup>
$\rho_{(fluid+CO_2)mix}$	1002.8 [44,45]	755.2 [46]	kg/m <sup>3</sup>
$\Delta\rho$	14.75	25.2	kg/m <sup>3</sup>
$D$	$3.643 \times 10^{-9}$ [47] **	$6 \times 10^{-9}$ [48] **	m <sup>2</sup> /s
$\mu$	$5.474 \times 10^{-4}$	$6.9 \times 10^{-4}$ [49]	kg/s·m

\* Obtained at 100 bar/50 °C; \*\* values were interpolated from given references of 100 bar/50 °C.

For the entire micromodel,  $Ra_{100\% \text{ water saturation}}$  and  $Ra_{100\% \text{ oil saturation}}$  were calculated as 60 and 36.5, respectively. In Case 2, the  $Ra$  with residual oil saturation ( $S_{or}$ ) was not calculated because there was no increase in the density of the fluid mixture (water and oil) due to  $CO_2$  mixing ( $\rho_{(fluid+CO_2)mix}$  value). Hence, the  $Ra$  number for Case 2 was assumed to be between  $Ra_{100\% \text{ water saturation}}$  and  $Ra_{100\% \text{ oil saturation}}$ .

### 3. Results and Discussion

Visualization results for the two experimental cases, as given in Table 2, are presented and discussed along with the analysis of images. In each experiment, the time (t) given on each image represents the start of the experiment (i.e., the time when  $CO_2$  injection into the micromodel stopped).

#### 3.1. Case 1: $CO_2$ Mixing in a 100% Water Saturation System

At the top of the micromodel, pores were more connected at the right side (see Figure 4b). Hence,  $CO_2$  initiated the mixing in water from the right side of the micromodel which was the preferential path. At the initiation,  $CO_2$  migrated into several pores at the top of the micromodel, which had more linked pores downwards. While  $CO_2$  was flowing via the preferential path (right side),  $CO_2$  was migrating toward less connected pores on the left side of the micromodel as well (follow  $CO_2$  path in Figures 8 and 9). Depending on the pore structure and pore location,  $CO_2$  was also transported horizontally (e.g., red circle at t = 7 min in Figure 8) and vertically upward (e.g., red circle at t = 31 min in Figure 9, which has an enlarged image in Figure 11). In the middle of the micromodel, more connected pores were located at the center. Hence, the main  $CO_2$  transport direction changed toward the middle part of the micromodel (see t = 119 min and t = 125 min in Figure 10). Meanwhile,  $CO_2$  migrated to the left and right sides (see white arrows at t = 131 min in Figure 10).

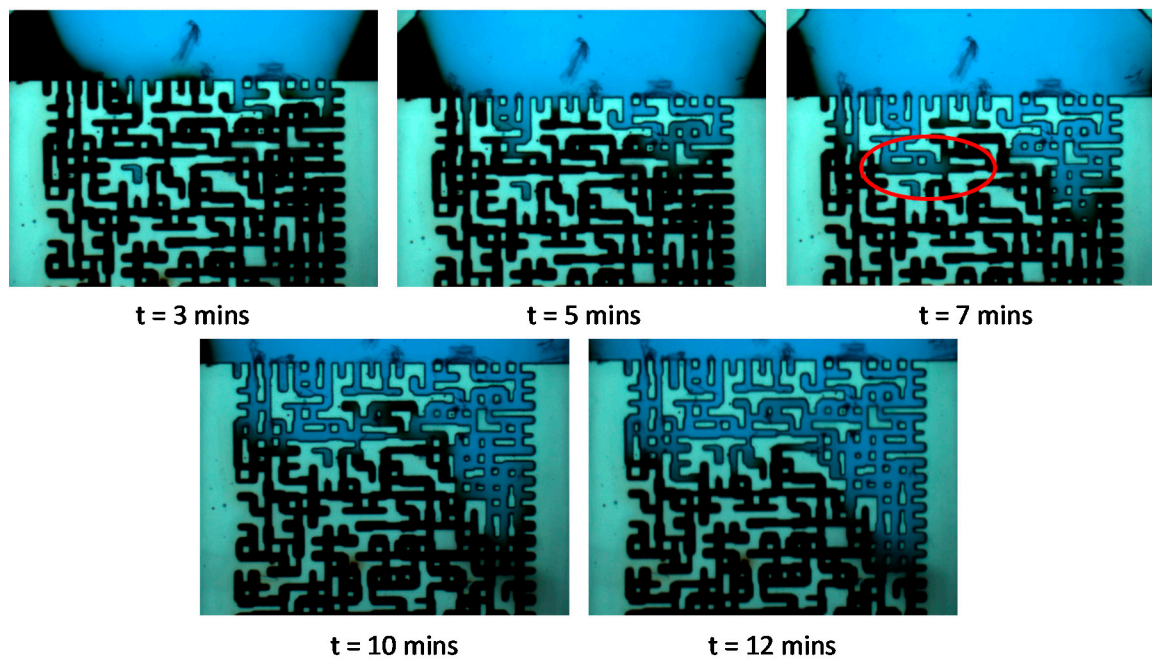


**Figure 8.** Initiation of CO<sub>2</sub> mixing from the top of the micromodel and propagation downwards, in Case 1.

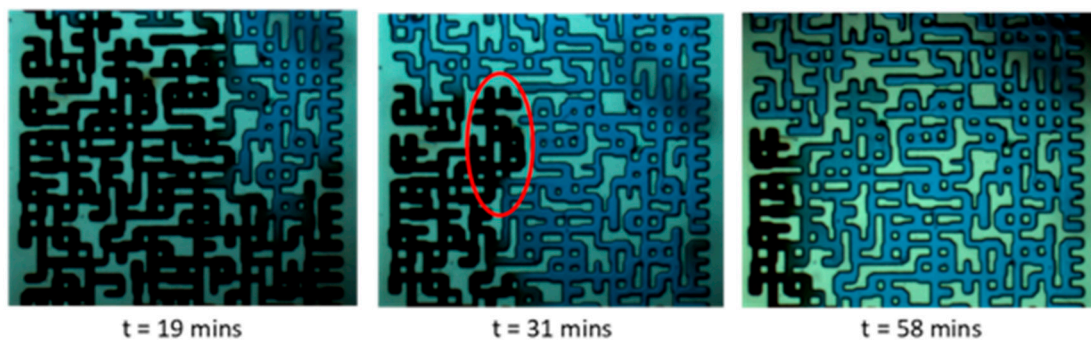


**Figure 9.** CO<sub>2</sub> transport inside the micromodel at a location 4–11 mm from the top of the micromodel, in Case 1.

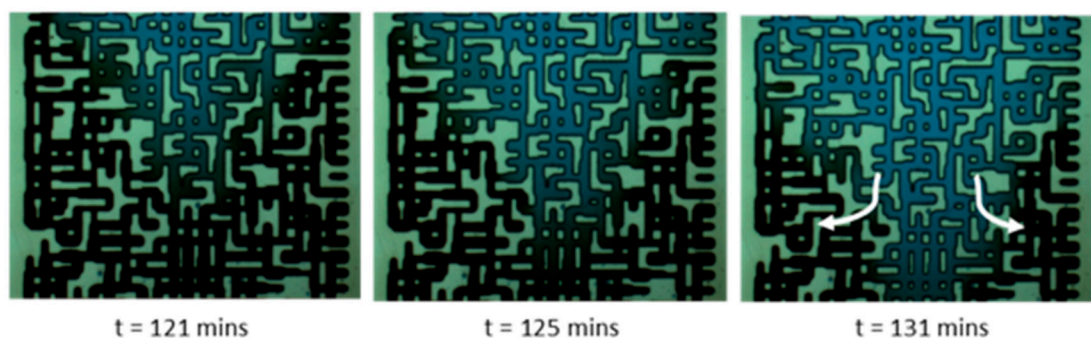


**Figure 10.** CO<sub>2</sub> transport inside the micromodel at a location 33–40 mm from the top of the micromodel, in Case 1.

Since the  $Ra$  number of the system is 60 and is higher than the  $Ra_{critical}$  value, the overall CO<sub>2</sub> mixing process through the connected pores is convective dominant. The average CO<sub>2</sub> transport velocity inside the micromodel, attributed to convection, was calculated to be  $0.3 \pm 3\%$  mm/min considering the time when CO<sub>2</sub> injection into the micromodel stopped and the breakthrough of CO<sub>2</sub>

into the bottom triangle occurred (i.e., CO<sub>2</sub> reaching the bottom triangle). The experimental setup of Case 1 was repeated twice, and similar velocities were calculated in both experiments. Although the CO<sub>2</sub> breakthrough occurred at the bottom, CO<sub>2</sub> was still invading the less connected pores inside the pore structure, as well as the dead-end pores.

At the location of 14.5 mm from the top of the micromodel, where pores were connected from the bottom, at  $t = 31$  min (see Figure 9 and enlarged images in Figure 11), the CO<sub>2</sub> invasion velocity upward was dampened. The CO<sub>2</sub> flow path is shown with a white arrow at  $t = 31$  min in Figure 11. At this particular location, the CO<sub>2</sub> velocity was calculated as 0.0975 mm/min upward (considering the time taken for CO<sub>2</sub> to travel the distance shown by the red arrow in Figure 11), which is approximately three times slower than the main CO<sub>2</sub> flux downwards through the micromodel. It is clear that the greater representation of the vertical upward-directed pores results in the deceleration of CO<sub>2</sub> dissolution. Furthermore, the local  $Ra$  value at this particular location was calculated as 3, assuming the same permeability. The  $Ra$  value is lower than the  $Ra_{critical}$  value, which indicates that the CO<sub>2</sub> flow at this location is diffusion dominant.

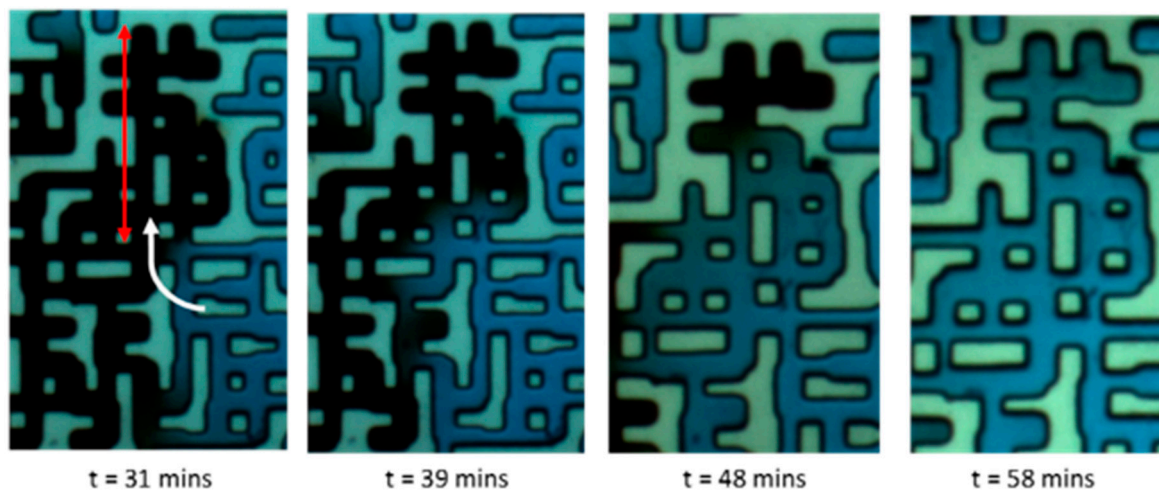


**Figure 11.** CO<sub>2</sub> mixing upward into dead-end pores located at 14.5 mm from the top of the micromodel in Case 1. Location identified by the red circle in Figure 9 at  $t = 31$  min.

CO<sub>2</sub> breakthrough at the bottom occurred first from the left side of the micromodel, which had more connected pores (see Figure 12). Then, CO<sub>2</sub> breakthrough was also observed from the right side. When CO<sub>2</sub> was transported from the pore structure into the free triangle, a couple of CO<sub>2</sub> convective fingers were observed (at  $t = 178$  min in Figure 12). With time, the fingers were merged, and CO<sub>2</sub> filled the triangle. Furthermore, additional dead-end pores were invaded, as shown in the red circle in Figure 12.

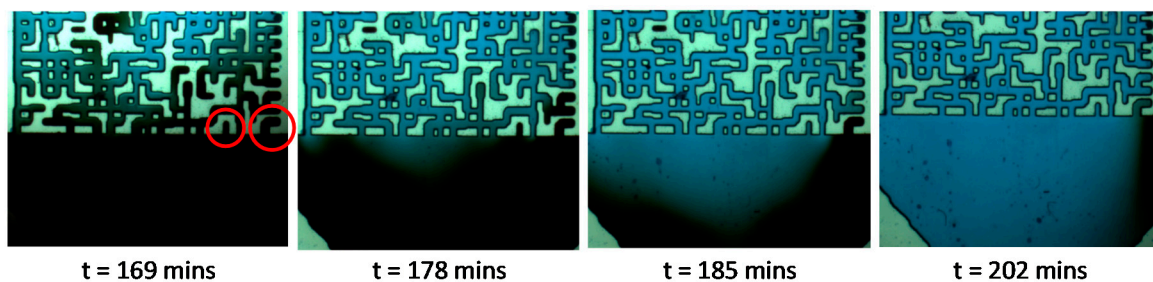


**Figure 12.** CO<sub>2</sub> breakthrough at the bottom of the micromodel, in Case 1.

### 3.2. Case 2: CO<sub>2</sub> Mixing in a Residual Oil-Saturated ( $S_{or}$ ) System

To the best of our knowledge, this is the first time a CO<sub>2</sub> convective mixing visualization experiment has been carried out in a three-phase system. As described in the experimental procedure, the entire micromodel was first established at  $S_{wi}$  (see Figure 13a) and, through water flooding,  $S_{or}$  was achieved (see Figure 13b). Then, CO<sub>2</sub> was introduced from the top of the micromodel.

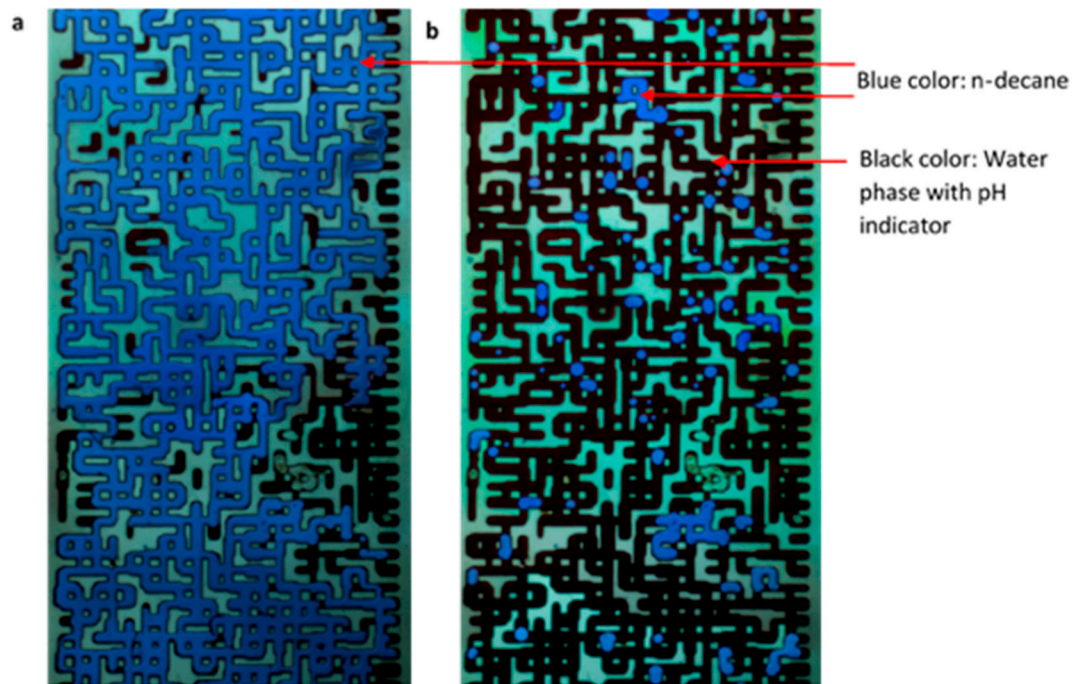


**Figure 13.** Micromodel image at location 10–25 mm at (a)  $S_{wi}$ ; (b)  $S_{or}$ , in Case 2.

Since CO<sub>2</sub> was injected into the micromodel before the pump was stopped, as described in the experimental procedure, the time stamps given in the images (Figures 14–16) started from the time when CO<sub>2</sub> injection into the micromodel was stopped. We observed that CO<sub>2</sub> was transported through oil ganglia and into the water phase again (see Figure 14 red circle locations). Similar effects have been observed in 2D experiments where CO<sub>2</sub> was transported through an oil layer and then into a water layer [25]. We also observed that the oil ganglia dampened the CO<sub>2</sub> transport velocity outside the main preferential path (e.g., sideways and toward dead-end pores) and CO<sub>2</sub> flow was more diffusion dominant. Figure 15 shows the CO<sub>2</sub> breakthrough at the bottom of the micromodel. Similar to Case 1 (100% water saturation), the breakthrough occurred at the right side of the micromodel (see Figure 15). The breakthrough at the right-side pores was slower than in Case 1, because the right side had fewer connected pores and the trapped oil ganglia dampened CO<sub>2</sub> transport inside the pores. The bulk average CO<sub>2</sub> transport velocity inside the micromodel, due to convection, was calculated to be  $0.3 \pm 3\%$  mm/min. This value was the same as in Case 1 (100% water saturation). Although the micromodel was at  $S_{or}$ , there was less oil remaining in the micromodel (see Figure 13b). Hence, there was less interruption of the downward CO<sub>2</sub> flow through the connected pores (preferential path) due to trapped oil, which led to a similar CO<sub>2</sub> transport velocity as in Case 1. The  $Ra$  value through the preferential path was assumed to be between 36.5 and 60, but closer to 60 due to low oil saturation. Hence, the overall CO<sub>2</sub> mixing process through the connected pores was convective dominant. Minimal oil swelling was observed, mainly due to the low  $S_{or}$ . Figure 16 shows how CO<sub>2</sub> was transported into some dead-end pores at the bottom of the micromodel (red circles). As shown by the arrow in Figure 16, at  $t = 70$  min, in the water phase, CO<sub>2</sub> was transported horizontally through the larger oil ganglia and invaded the dead-end pores located upward with a velocity of  $0.12 \pm 3\%$  mm/min (velocity calculated considering the time taken for CO<sub>2</sub> to be transported the distance of the white arrow shown in Figure 16).

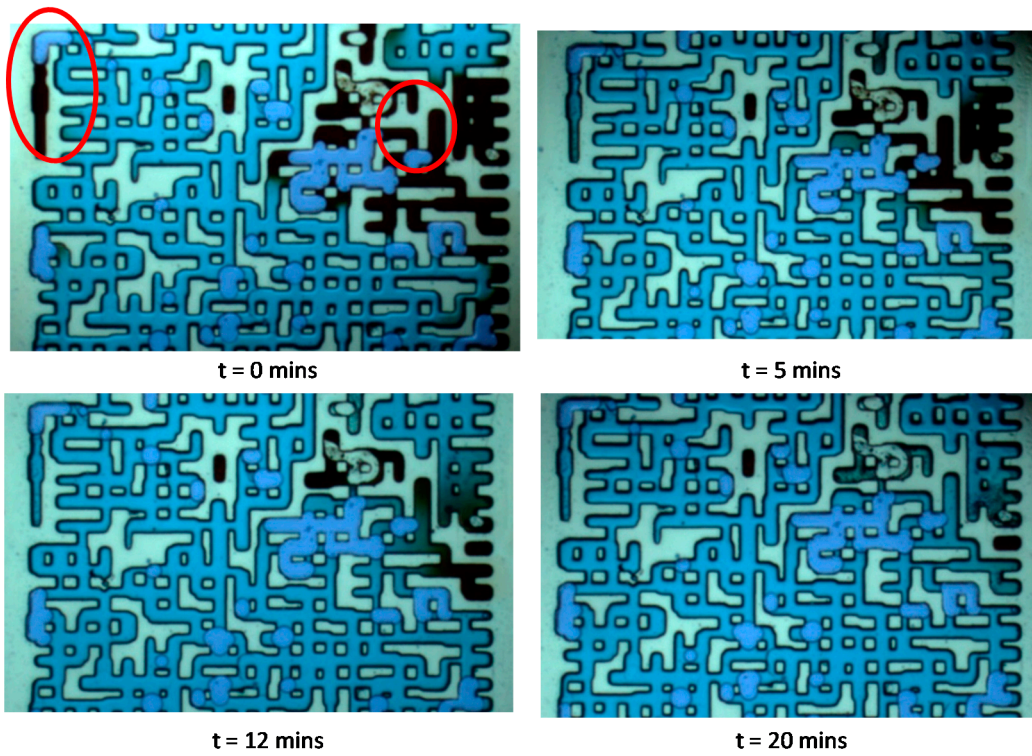


**Figure 14.** CO<sub>2</sub> invading dead-end pores through oil ganglia in the water phase (focused points in red circle), in Case 2 experiment. Location at 19–24 cm from the top.

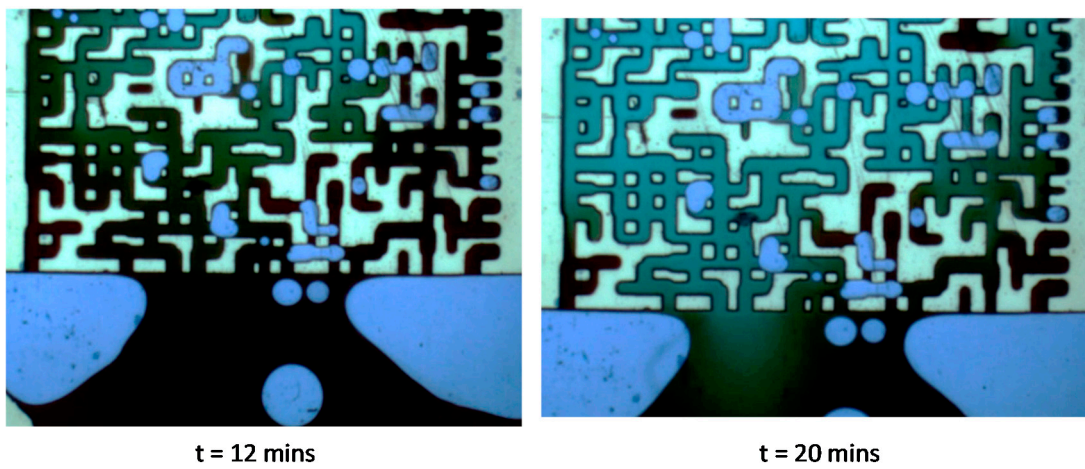


**Figure 15.** CO<sub>2</sub> breakthrough from the bottom, in Case 2.

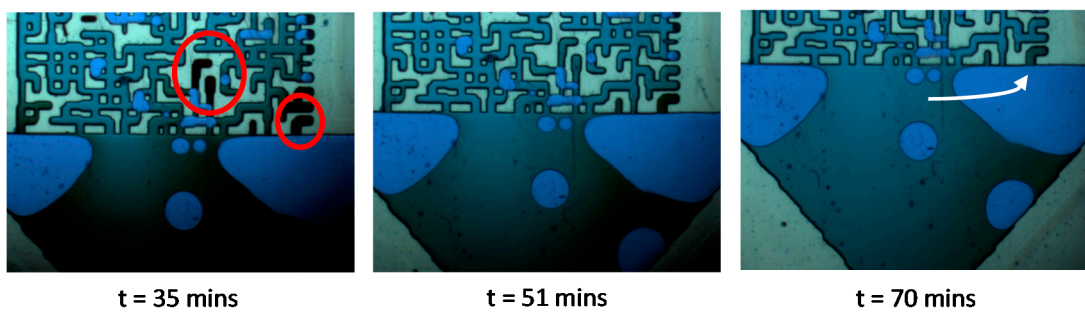


**Figure 16.** CO<sub>2</sub> invading water-saturated dead-end pores through the oil, in Case 2.

### 3.3. General Discussion

Due to the low volume ( $0.01 \text{ cm}^3$ ) of the micromodel, establishing initial conditions was challenging. A recognizable pressure head (e.g., 0.01 bar) deviation was found due to the fact that  $\text{CO}_2$  in the connected tubes of the micromodel might have led to an external influence on  $\text{CO}_2$  transport. This error can influence  $\text{CO}_2$  transport velocity inside a micromodel, where the real  $\text{CO}_2$  transport velocity value is slightly lower than the estimated values.

$\text{CO}_2$  convective mixing in water-saturated porous media at the same temperature ( $50 \text{ }^\circ\text{C}$ ) and pressure conditions (100 bar) has been previously reported by Amarasinghe, et al. [22] through experiments inside a 2D Hele-Shaw cell. The experiments were conducted with 4D and 76D permeability of the porous media and the  $\text{CO}_2$  transport velocity was calculated to be 0.04 mm/min and 1.83 mm/min, respectively. The experimental setup by Amarasinghe, et al. [22] used a circular boundary and a larger quantity of porous media. Therefore, the  $\text{CO}_2$  transport velocities cannot be directly compared with our micromodel results, but the micromodel experiments showed that the  $\text{CO}_2$  transport at a pore-scale level behaved differently as compared with 2D experiments.

We did not observe  $\text{CO}_2$  convective fingering inside the pores of the micromodel experiments described above, except in the top and bottom triangles. This was due to the narrow width of the micromodel, which was smaller than the wavelength of the fingers observed by Amarasinghe, et al. [22] and Mahmoodpour, et al. [24]. Furthermore, at a pore-scale level,  $\text{CO}_2$  is always transported through the connected pores, which reduces the chances of generating convective fingers.

## 4. Future Work

The results presented are important for estimating  $\text{CO}_2$  mixing time with underground fluids for existing and planned  $\text{CO}_2$  storage projects. Importantly, these visualization data are important for the development and validation of numerical simulation models. An existing 2D model's grid could be altered according to the micromodel pore structure and the data could be used to validate the models [12,13]. We suggest those modeling activities be carried out in future work. Furthermore, we suggest conducting similar experiments with different pore structures and with different pressure and temperature conditions. We also suggest investigating the effects of head pressure using different injection rates for  $\text{CO}_2$  injection into a micromodel. It is suspected that, due to low volume in the micromodel, small head pressure deviations might be having a significant effect on the  $\text{CO}_2$  transport rate.

## 5. Conclusions

On the basis of the results from a micromodel study of  $\text{CO}_2$  mixing at 100% water saturation and residual oil-saturated reservoir conditions, the following conclusions can be drawn:

- $\text{CO}_2$  always found the easiest path through connected pores during mixing, and then  $\text{CO}_2$  was transported into less connected pores and dead-end pores.
- $\text{CO}_2$  transport into dead-end pores was slower than  $\text{CO}_2$  flow through the preferential path.
- We observed how  $\text{CO}_2$  was transported through trapped oil ganglia and into the water phase again. It was also observed that oil ganglia dampened the  $\text{CO}_2$  transport velocity outside the main preferential path.
- $\text{CO}_2$  mixing into dead-end pores and less connected pores was diffusion dominant.

**Author Contributions:** Conceptualization, W.A., S.F., I.F., M.S., and Y.G.; methodology, W.A., S.F., and M.S.; validation, W.A.; formal analysis, W.A. and I.F.; investigation, W.A., S.F., and I.F.; resources, M.S. and Y.G.; writing—original draft preparation, W.A., S.F., and I.F.; writing—review and editing, W.A., I.F., and Y.G.; visualization, W.A. and S.F.; supervision, I.F., M.S., and Y.G.; project administration, Y.G.; funding acquisition, Y.G. All authors have read and agreed to the published version of the manuscript.

**Funding:** Research Council of Norway, CLIMIT program, grant number 268439.

**Institutional Review Board Statement:** Not applicable.

**Informed Consent Statement:** Not applicable.

**Data Availability Statement:** All data are given in the paper (there are no other data).

**Acknowledgments:** Authors would like to acknowledge the laboratory staff at the Centre for Enhanced Oil Recovery and CO<sub>2</sub> Solutions, Heriot-Watt University, Edinburgh, United Kingdom, for the support given during the experiments.

**Conflicts of Interest:** The authors declare no conflict of interest. The funders had no role in the design of the study; in the collection, analyses, or interpretation of data; in the writing of the manuscript, or in the decision to publish the results.

## References

1. Holt, T.; Jensen, J.I.; Lindeberg, E. Underground Storage of CO<sub>2</sub> in Aquifers and Oil Reservoirs. *Energy Convers. Manag.* **1995**, *36*, 535–538. [[CrossRef](#)]
2. Hendriks, C.A.; Blok, K. Underground Storage of Carbon Dioxide. *Energy Convers. Manag.* **1993**, *34*, 949–957. [[CrossRef](#)]
3. Ringrose, P. *How to Store CO<sub>2</sub> Underground: Insights from Early-Mover CCS Projects*; Springer International Publishing: Berlin/Heidelberg, Germany, 2020; p. 129.
4. Rackley, S.A. Chapter 11—Geological Storage. In *Carbon Capture and Storage*; Rackley, S.A., Ed.; Butterworth-Heinemann: Boston, MA, USA, 2010; pp. 227–266.
5. Aminu, M.D.; Nabavi, S.A.; Rochelle, C.A.; Manovic, V. A Review of Developments in Carbon Dioxide Storage. *Appl. Energy* **2017**, *208*, 1389–1419. [[CrossRef](#)]
6. Freund, P.; Ormerod, W.G. Progress Toward Storage of Carbon Dioxide. *Energy Convers. Manag.* **1997**, *38*, 199–204. [[CrossRef](#)]
7. Kuuskraa, V.A.; Godec, M.L.; Dipietro, P. CO<sub>2</sub> Utilization from “Next Generation” CO<sub>2</sub> Enhanced Oil Recovery Technology. *Energy Procedia* **2013**, *37*, 6854–6866. [[CrossRef](#)]
8. Roefs, P.; Moretti, M.; Welkenhuysen, K.; Piessens, K.; Compernelle, T. CO<sub>2</sub>-Enhanced Oil Recovery and CO<sub>2</sub> Capture and Storage: An Environmental Economic Trade-Off Analysis. *J. Environ. Manag.* **2019**, *239*, 167–177. [[CrossRef](#)]
9. Emami-Meybodi, H.; Hassanzadeh, H.; Green, C.P.; Ennis-King, J. Convective Dissolution of CO<sub>2</sub> in Saline Aquifers: Progress in Modeling and Experiments. *Int. J. Greenh. Gas Control* **2015**, *40*, 238–266. [[CrossRef](#)]
10. Lindeberg, E.; Wessel-Berg, D. Vertical Convection in an Aquifer Column Under a Gas Cap of CO<sub>2</sub>. *Energy Convers. Manag.* **1997**, *38*, S229–S234. [[CrossRef](#)]
11. Gasda, S.E.; Elenius, M.T.; Kaufmann, R. Field-Scale Implications of Density-Driven Convection in CO<sub>2</sub>-EOR Reservoirs. In Proceedings of the Fifth CO<sub>2</sub> Geological Storage Workshop, Utrecht, The Netherlands, 21–23 November 2018; pp. 1–5. [[CrossRef](#)]
12. Both, J.; Gasda, S.; Aavatsmark, I.; Kaufmann, R. Gravity-driven Convective Mixing of CO<sub>2</sub> in Oil. In Proceedings of the Third Sustainable Earth Sciences Conference and Exhibition, Celle, Germany, 13–15 October 2015; pp. 1–5. [[CrossRef](#)]
13. Gasda, S.; Elenius, M.T. CO<sub>2</sub> Convection in Oil Driven by Non-Monotonic Mixture Density. In Proceedings of the ECMOR XVI—16th European Conference on the Mathematics of Oil Recovery, Barcelona, Spain, 3–6 September 2018; pp. 1–12. [[CrossRef](#)]
14. Elenius, M.T.; Nordbotten, J.M.; Kalisch, H. Convective Mixing Influenced by the Capillary Transition Zone. *Comput. Geosci.* **2014**, *18*, 417–431. [[CrossRef](#)]
15. Farajzadeh, R.; Salimi, H.; Zitha, P.L.J.; Bruining, H. Numerical Simulation of Density-Driven Natural Convection in Porous Media with Application for CO<sub>2</sub> Injection Projects. *Int. J. Heat Mass Transf.* **2007**, *50*, 5054–5064. [[CrossRef](#)]
16. Teng, Y.; Wang, P.; Liu, Y.; Jiang, L.; Wang, D. A Spectrophotometric Method for Measuring Dissolved CO<sub>2</sub> in Saline Water. *Exp. Fluids* **2018**, *59*, 138. [[CrossRef](#)]
17. Faisal, T.F.; Chevalier, S.; Bernabe, Y.; Juanes, R.; Sassi, M. Quantitative and Qualitative Study of Density Driven CO<sub>2</sub> Mass Transfer in a Vertical Hele-Shaw Cell. *Int. J. Heat Mass Transf.* **2015**, *81*, 901–914. [[CrossRef](#)]
18. Khosrokhavar, R.; Elsinga, G.; Farajzadeh, R.; Bruining, H. Visualization and Investigation of Natural Convection Flow of CO<sub>2</sub> in Aqueous and Oleic Systems. *J. Pet. Sci. Eng.* **2014**, *122*, 230–239. [[CrossRef](#)]

19. Kneafsey, T.J.; Pruess, K. Laboratory Flow Experiments for Visualizing Carbon Dioxide-Induced, Density-Driven Brine Convection. *Transp. Porous Media* **2010**, *82*, 123–139. [[CrossRef](#)]
20. Lu, G.; Liu, Y.; Jiang, L.; Ying, T.; Song, Y.; Wu, B. Study of Density Driven Convection in a Hele-Shaw Cell with Application to the Carbon Sequestration in Aquifers. *Energy Procedia* **2017**, *114*, 4303–4312. [[CrossRef](#)]
21. Thomas, C.; Dehaeck, S.; De Wit, A. Convective Dissolution of CO<sub>2</sub> in Water and Salt Solutions. *Int. J. Greenh. Gas Control* **2018**, *72*, 105–116. [[CrossRef](#)]
22. Amarasinghe, W.; Fjelde, I.; Rydland, J.-Å.; Guo, Y. Effects of Permeability on CO<sub>2</sub> Dissolution and Convection at Reservoir Temperature and Pressure Conditions: A Visualization Study. *Int. J. Greenh. Gas Control* **2020**, *99*, 103082. [[CrossRef](#)]
23. Vosper, H.; Kirk, K.; Rochelle, C.; Noy, D.; Chadwick, A. Does Numerical Modelling of the Onset of Dissolution-convection Reliably Reproduce this Key Stabilization Process in CO<sub>2</sub> Storage? *Energy Procedia* **2014**, *63*, 5341–5348. [[CrossRef](#)]
24. Mahmoodpour, S.; Rostami, B.; Soltanian, M.R.; Amooie, M.A. Effect of Brine Composition on the Onset of Convection During CO<sub>2</sub> Dissolution in Brine. *Comput. Geosci.* **2019**, *124*, 1–13. [[CrossRef](#)]
25. Amarasinghe, W.S.; Fjelde, I.; Guo, Y. CO<sub>2</sub> Dissolution and Convection in Oil at Realistic Reservoir Conditions: A Visualization Study. *J. Nat. Gas Sci. Eng.* **2021**. under review.
26. Sun, Y.; Kharaghani, A.; Tsotsas, E. Micro-Model Experiments and Pore Network Simulations of Liquid Imbibition in Porous Media. *Chem. Eng. Sci.* **2016**, *150*, 41–53. [[CrossRef](#)]
27. Song, Y.; Zhao, C.; Chen, M.; Chi, Y.; Zhang, Y.; Zhao, J. Pore-Scale Visualization Study on CO<sub>2</sub> Displacement of Brine in Micromodels with Circular and Square Cross Sections. *Int. J. Greenh. Gas Control* **2020**, *95*, 102958. [[CrossRef](#)]
28. Mahzari, P.; Sohrabi, M.; Cooke, A.J.; Carnegie, A. Direct Pore-Scale Visualization of Interactions Between Different Crude Oils and Low Salinity Brine. *J. Pet. Sci. Eng.* **2018**, *166*, 73–84. [[CrossRef](#)]
29. Romero-Zeron, L.; Kantzas, A. Pore-Scale Visualization of Foamed Gel Propagation and Trapping in a Pore Network Micromodel. *Petsoc-99-07-02* **2005**, *44*, 7. [[CrossRef](#)]
30. Emadi, A.; Sohrabi, M. Visual Investigation of Oil Recovery by Low Salinity Water Injection: Formation of Water Micro-Dispersions and Wettability Alteration. In Proceedings of the SPE Annual Technical Conference and Exhibition, New Orleans, LA, USA, 30 September 2013; p. 15. [[CrossRef](#)]
31. Sohrabi, M.; Henderson, G.D.; Tehrani, D.H.; Danesh, A. Visualisation of Oil Recovery by Water Alternating Gas (WAG) Injection Using High Pressure Micromodels—Water-Wet System. In Proceedings of the SPE Annual Technical Conference and Exhibition, Dallas, TX, USA, 1–4 October 2000; p. 8. [[CrossRef](#)]
32. Campbell, B.T.; Orr, F.M., Jr. Flow Visualization for CO<sub>2</sub>/Crude-Oil Displacements. *SPE-6192-PA* **1985**, *25*, 665–678. [[CrossRef](#)]
33. Hatiboglu, C.U.; Babadagli, T. Pore-Scale Studies of Spontaneous Imbibition into Oil-Saturated Porous Media. *Phys. Rev. E* **2008**, *77*, 066311. [[CrossRef](#)]
34. Robin, M.; Behot, J.; Sygouni, V. CO<sub>2</sub> Injection in Porous Media: Observations in Glass Micromodels Under Reservoir Conditions. In Proceedings of the SPE Improved Oil Recovery Symposium, Tulsa, OK, USA, 14–18 April 2012; p. 15. [[CrossRef](#)]
35. Farzaneh, S.A.; Sohrabi, M. Visual Investigation of Improvement in Extra-Heavy Oil Recovery by Borate-Assisted CO<sub>2</sub>-Foam Injection. *Transp. Porous Media* **2018**, *122*, 487–513. [[CrossRef](#)]
36. Farzaneh, S.A.; Kharrat, R.; Ghazanfari, M.H. Experimental Study of Solvent Flooding to Heavy Oil in Fractured Five-Spot Micro-Models: The Role of Fracture Geometrical Characteristics. *Petsoc-99-07-02* **2010**, *49*, 36–43. [[CrossRef](#)]
37. Zhang, C.; Oostrom, M.; Grate, J.W.; Wietsma, T.W.; Warner, M.G. Liquid CO<sub>2</sub> Displacement of Water in a Dual-Permeability Pore Network Micromodel. *Environ. Sci. Technol.* **2011**, *45*, 7581–7588. [[CrossRef](#)]
38. Sell, A.; Fadaei, H.; Kim, M.; Sinton, D. Measurement of CO<sub>2</sub> Diffusivity for Carbon Sequestration: A Microfluidic Approach for Reservoir-Specific Analysis. *Environ. Sci. Technol.* **2013**, *47*, 71–78. [[CrossRef](#)]
39. Liu, N.; Aymonier, C.; Lecoutre, C.; Garrabos, Y.; Marre, S. Microfluidic Approach for Studying CO<sub>2</sub> Solubility in Water and Brine Using Confocal Raman Spectroscopy. *Chem. Phys. Lett.* **2012**, *551*, 139–143. [[CrossRef](#)]
40. Morais, S.; Cario, A.; Liu, N.; Bernard, D.; Lecoutre, C.; Garrabos, Y.; Ranchou-Peyruse, A.; Dupraz, S.; Azaroual, M.; Hartman, R.L.; et al. Studying Key Processes Related to CO<sub>2</sub> Underground Storage at the Pore Scale Using High Pressure Micromodels. *React. Chem. Eng.* **2020**, *5*, 1156–1185. [[CrossRef](#)]

41. Sohrabi, M.; Tehrani, D.H.; Danesh, A.; Henderson, G.D. Visualization of Oil Recovery by Water-Alternating-Gas Injection Using High-Pressure Micromodels. *SPE-89000-PA* **2004**, *9*, 290–301. [[CrossRef](#)]
42. Rueden, C.T.; Schindelin, J.; Hiner, M.C.; DeZonia, B.E.; Walter, A.E.; Arena, E.T.; Eliceiri, K.W. ImageJ2: ImageJ for the Next Generation of Scientific Image Data. *BMC Bioinform.* **2017**, *18*, 529. [[CrossRef](#)]
43. Ennis-King, J.P.; Paterson, L. Role of Convective Mixing in the Long-Term Storage of Carbon Dioxide in Deep Saline Formations. *SPE-89000-PA* **2005**, *10*, 349–356. [[CrossRef](#)]
44. Hebach, A.; Oberhof, A.; Dahmen, N. Density of Water + Carbon Dioxide at Elevated Pressures: Measurements and Correlation. *J. Chem. Eng. Data* **2004**, *49*, 950–953. [[CrossRef](#)]
45. Efika, E.C.; Hoballah, R.; Li, X.; May, E.F.; Nania, M.; Sanchez-Vicente, Y.; Martin Trusler, J.P. Saturated Phase Densities of (CO<sub>2</sub> + H<sub>2</sub>O) at Temperatures from (293 To 450)K and Pressures up to 64 MPa. *J. Chem. Thermodyn.* **2016**, *93*, 347–359. [[CrossRef](#)]
46. Song, Y.; Jian, W.; Zhang, Y.; Shen, Y.; Zhan, Y.; Zhao, J.; Liu, Y.; Wang, D. Densities and Volumetric Characteristics of Binary System of CO<sub>2</sub> + Decane from (303.15 to 353.15) K and Pressures up to 19 MPa. *J. Chem. Eng. Data* **2012**, *57*, 3399–3407. [[CrossRef](#)]
47. Cadogan, S.P.; Maitland, G.C.; Trusler, J.P.M. Diffusion Coefficients of CO<sub>2</sub> and N<sub>2</sub> in Water at Temperatures between 298.15 K and 423.15 K at Pressures up to 45 MPa. *J. Chem. Eng. Data* **2014**, *59*, 519–525. [[CrossRef](#)]
48. Cadogan, S.P.; Mistry, B.; Wong, Y.; Maitland, G.C.; Trusler, J.P.M. Diffusion Coefficients of Carbon Dioxide in Eight Hydrocarbon Liquids at Temperatures between (298.15 and 423.15) K at Pressures up to 69 MPa. *J. Chem. Eng. Data* **2016**, *61*, 3922–3932. [[CrossRef](#)]
49. Lee, A.L.; Ellington, R.T. Viscosity of n-Decane in the Liquid Phase. *J. Chem. Eng. Data* **1965**, *10*, 346–348. [[CrossRef](#)]

**Publisher's Note:** MDPI stays neutral with regard to jurisdictional claims in published maps and institutional affiliations.



© 2021 by the authors. Licensee MDPI, Basel, Switzerland. This article is an open access article distributed under the terms and conditions of the Creative Commons Attribution (CC BY) license (<http://creativecommons.org/licenses/by/4.0/>).